An endoscopic structured light system using multispectral detection

Jianyu Lin[1,2], Neil T. Clancy[1,3], Daniel S. Elson[1,3]

[1] *Hamlyn Centre for Robotic Surgery, Institute of Global Health Innovation, Imperial College London, SW7 2AZ, UK*

[2] *Department of Computing, Imperial College London, SW7 2AZ, UK*

[3] *Department of Surgery and Cancer, Imperial College London, SW7 2AZ, UK*

j.lin12@imperial.ac.uk

Abstract

Purpose In clinical examinations, the tissue surface topology is an important feature for detecting the tissue pathology and implementing augmented reality. We have previously presented a miniaturised structured light (SL) system for recovery of tissue surface shape in minimally invasive surgery (MIS), based on a flexible multispectral structured illumination probe (1.9 mm diameter) [1]. This paper reports further hardware and analytical developments to improve the light pattern decoding result and increase the reconstruction accuracy.

Methods The feasibility of using an 8-band multispectral camera with higher pattern-colour discrimination ability than normal RGB camera in this system was studied. Additionally, the "normalized cut" algorithm was investigated to improve pattern segmentation.

Results The whole SL system was evaluated by phantom and *in vivo* experiments. Higher pattern identification performance than that of an RGB camera was recorded by using the multispectral camera (average precision > 97%, average sensitivity > 62%). An average of 0.88±0.67 mm reconstruction error was achieved using the proposed pattern decoding method on a heart phantom at a working distance of approximately 10 cm.

Conclusions The experiment showed the superiority of the multispectral camera over the RGB camera in the spot identification step. The proposed pattern decoding algorithm underwent evaluations using different experiments, showing that it provided promising reconstruction results. The potential of using this system in MIS environments has been demonstrated.

Keywords: *structured light, endoscopy, multispectral camera, light pattern decoding, reconstruction*

1 Introduction

1.1 Tissue surface reconstruction using structured light

The quantification of tissue surface morphology is of high importance in medicine and surgery as it may be sensitive to tissue pathology. For instance, the detection

of colonic polyps often depends on their shape, with flat polyps being much less visible under conventional illumination [2]. Also, tissue surface shape has potential to be used in MIS to facilitate navigation. Optical techniques for surface detection may allow pre-operative information, for instance from imaging modalities such as MRI, CT, or ultrasound, to provide augmented reality for surgical guidance [3,4].

Among all the optical techniques used for 3D reconstruction, SL has good potential to be used in surgical environments as they have the advantage of performing well even on relatively featureless objects [3]. In SL, a setup is designed to generate a specific artificial light pattern and project it onto the target object. Then according to the location of the projected light pattern recorded by a single camera, the object surface is reconstructed. Prior to the 3D reconstruction a geometrical calibration is conducted to establish the spatial relationship between the projector and camera. The pattern should be structured so that for any specific part of it its corresponding projected ray may be identified in the calibration dataset. SL systems can be divided into two types: multi-shot and single-shot. Multi-shot SL uses a sequence of patterns to assign unique codewords to different object surface areas, while single-shot only projects one light encoding pattern [5]. The former generally leads to denser reconstruction but suffers from long image acquisition time, while the latter normally results in sparser reconstruction but faster acquisition. Therefore, the single-shot pattern is more suitable for the application of 3D reconstruction during surgery where the tissue may constantly move. Some examples of single-shot patterns include Ackerman et al., who designed and enhanced their laparoscopic SL system using a coded stripe pattern for abdominal organ imaging [6]. Chan et al. proposed another endoscopic SL system which uses a single-shot dot matrix as the projection pattern [7]. For the purpose of improving accuracy of cervical cancer diagnosis during colposcopy, another system used a grid pattern to reconstruct the tissue surface [8]. Recently, Maurice et al. developed a rigid laparoscopic system with a single-shot grid-based pattern designed according to the M-array (perfect maps) algorithm [9]. Another recent single-shot endoscopic SL system was developed by Schmalz et al. [10]. This scanner was specially designed for tissue reconstruction in tubular cavities, so a camera with a curved mirror, and a ring-shaped slide projector were designed to produce and record ring-like patterns.

1.2 The ICL SL system

A unique system (ICL SL system) has been proposed by our group [1]. Briefly, a 4 W supercontinuum laser (420-750 nm) was dispersed by an SF-11 prism before being focussed onto a linear array of 127 fibres. Those fibres, each carrying light of a unique narrowband spectrum, pass through a custom-made converter to form a random distribution distally. A gradient refractive index (GRIN) objective lens forms an image of the bundle end-face resulting in a random spot pattern. The brass ferrule of the fibre linear array has a diameter of 12.5 mm, but the fibre bundle and distal tip of the probe has a maximum outer diameter of 1.9 mm, making it compatible with biopsy channels of many flexible and rigid endoscopes. The region of interest (ROI) increases as the working distance increases. A typical 10 cm^2 ROI can be acquired at a working distance of 10 cm. The system schematic and the projected pattern are shown in Fig. 1.

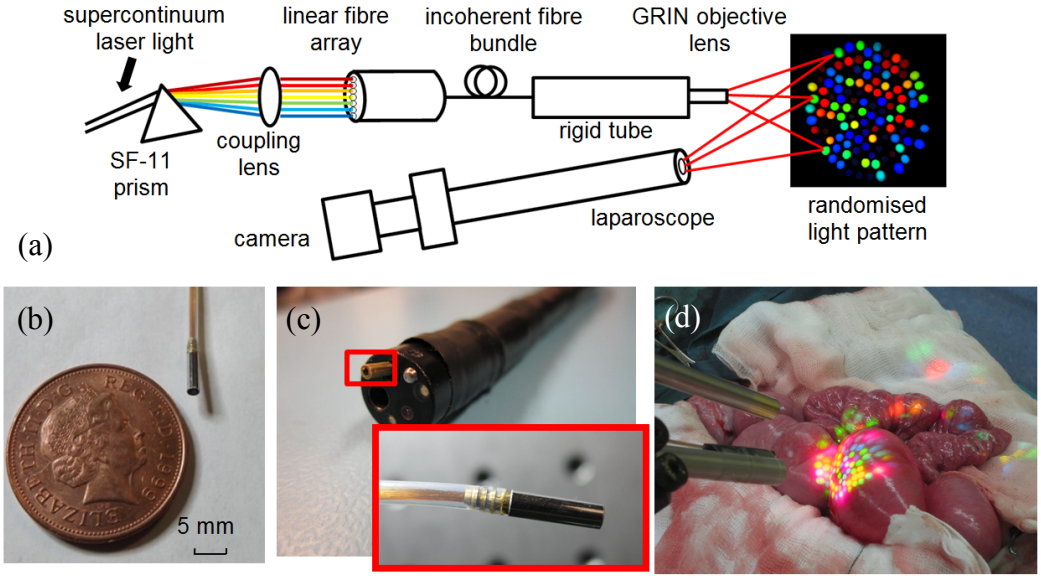

Fig. 1. (a) Schematic of the ICL SL system. (b) The miniaturised probe tip. (c) The probe inserted through the biopsy channel of a colonoscope. (d) *In vivo* porcine large bowel under SL.

Despite its advantages, this system has limitations in real applications. One of the limitations is light pattern decoding. If an RGB camera is adopted, the reconstruction accuracy is limited to those wavelengths falling in the overlapping area between transmission spectra of the camera's Bayer filter (blue/green, green/red). In other regions, however, spots with similar wavelengths cannot always be differentiated unambiguously, due to the monochromatic response of the camera. Furthermore, at the blue end of the spectrum light is absorbed strongly by molecules like haemoglobin, while higher penetration depth at the red

end results in increased lateral diffusion and a decrease in edge contrast when projected onto the tissue surface. All of the above problems lead to increased difficulty of pattern decoding.

1.3 Sequential multispectral imaging

As an image acquisition technique, sequential multispectral imaging (MSI) captures images of certain objects at diverse wavelengths, compiling spectra for all the pixels. This technique is used in a number of medical applications. For instance, chromophores like oxy- and deoxyhaemoglobin can be detected and differentiated, and their relative concentrations used to determine measures of tissue perfusion and oxygen saturation [11,12]; molecular targeting and spectral unmixing of multiple fluorophores can also be achieved using multispectral fluorescence imaging [13,14]. Compared to normal RGB cameras, which only record three wavebands, a multispectral camera results in images corresponding to more wavelengths, providing higher colour discrimination ability. However, according to our knowledge, there is no work in which a multispectral camera is integrated with an SL system.

1.4 Achievement of this work

We aim to apply the ICL SL system in clinical applications. Thus, this paper focuses on two aspects: the feasibility evaluation of the multispectral camera and the development of the light pattern decoding algorithm. Phantom, *ex vivo*, and *in vivo* experiments were used for the evaluation. In order to make full use of the colour information to facilitate the decoding procedure, a multispectral camera is used instead of a normal RGB camera, showing a better performance in the *in vivo* experiment. Together with its extra medical diagnostic applications during surgery, the multispectral camera demonstrates potential to be adapted to the current SL system. Furthermore, a robust and promising light pattern decoding algorithm is proposed and evaluated on phantoms and *in vivo*. This algorithm includes spot segmentation and spot identification. In the former step, an algorithm based on the H-maxima transform [15] and “normalized cut” [16] is used to delineate the spots and find their centroids. Colour and neighbourhood information are considered as criteria to identify the spots, using a “labelling propagation” technique based on local rigid registration.

2 Methods

2.1 SL system Calibration

Calibration is an essential step in computer vision to extract 3D information from 2D images. Similarly, the calibration of our SL system can be divided into two steps: camera calibration and projector calibration.

Geometrical camera calibration is a very mature technique which is based on homography, and its detailed procedure can be found in previous works [17,18]. Projector calibration of our SL system is also based on homography. The projector is considered to be an inverse pinhole camera model without distortion. Given that a sparse light pattern is used in this project, and one spot on the SL image indicates the intersection position between the object surface and one ray from the projector, to calibrate the projector means to find the directions of all the rays from the probe. In this procedure a "hollow pattern" checkerboard is used (Fig. 2 (a)). During calibration this checkerboard is manually positioned at different distances from the projector.

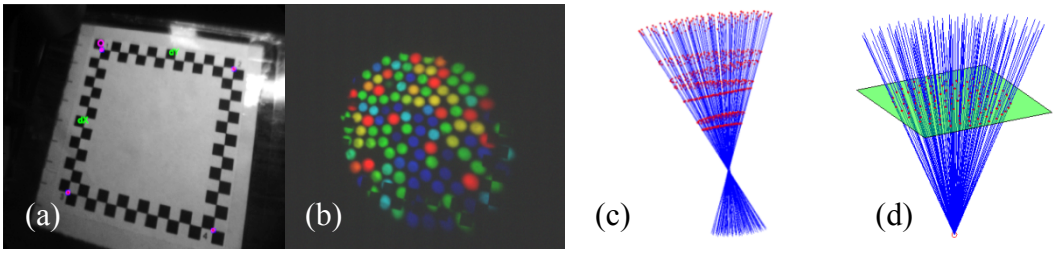

Fig. 2. (a) "Hollow" checkerboard. (b) SL image on the checkerboard. (c) Locations of spots in different plane positions (red); rays estimated by line fitting (blue). (d) The projector model: rays (blue line), projector image plane (green), coordinates of features (red dots) on the image plane; the probe centre (red circle).

At the i^{th} position, both white light and SL images are taken (Fig. 2 (a, b)). According to the homography based on a rectangle formed by any four corners on it, the orientation and position of the checkerboard can be calculated in terms of a rotation matrix R_i and the coordinate of one point on the plane M_i. For a ray P_{ij} represented by a certain spot S_j, its direction P_{ij} can be estimated from the known R_i and M_i by intersection. Assuming the checkerboard has been located in N positions, and there are 127 spots/rays in total, then P_{ij} is computed with all $i \in (1, \dots, N)$ and $j \in (1, \dots, 127)$. As a result, N coordinates are acquired for all the spots/rays. Then a line fitting algorithm is applied, estimating all the ray

directions (Fig. 2 (c)). Next, an optimisation technique is applied to force all the rays go through one point which approximates the projector centre (Fig. 2 (d)).

Given the calibration results, the object surface can be reconstructed using the image coordinates of the spot centroids. In the following, we present a light pattern decoding algorithm to locate the spot centroids.

2.2 Colour representation

Colour is the most important feature for light pattern decoding using this SL system. The collected SL images contain multiple components, each representing the colour image in a certain wavelength band. Therefore, there are several colour components for one single pixel, the quantity of which depends on the camera used. In this work, "colour vectors" are utilised to represent colours for pixels. A colour vector is a unit vector defined by the normalised magnitude of each colour component. In a process similar to that used in spectral angle mapping [19] the difference between two pixels i and j can be quantified by the angle θ between their corresponding colour vectors C_i and C_j, ranging from 0° to 90°:

$$\theta_{ij} = \cos^{-1} \frac{C_i \,.\, C_j}{\|C_i\| * \|C_j\|} \tag{1}$$

Using the angle as the only indicator to describe the colour difference brings convenience to the following light pattern decoding procedure.

2.3 Multispectral camera

In this project, two types of camera are used to capture the SL image. One is a standard colour CCD camera (DCU 223C, Thorlabs Ltd., UK), which has three channels of output, indicating three different wavebands in the blue, green and red ranges, respectively. However, as is shown in Fig. 3 (b), only those overlapping areas between different filter transmission spectra have the potential to be used to distinguish those spots, since the ratio of corresponding transmission values of adjacent filters is sensitive to the wavelength change. In order to increase the overlapping spectral area, a multispectral camera (SpectroCam, Pixelteq, Florida, USA) was applied in this paper, which contains eight different bandpass filters, leading to eight channels in the output images. Fig. 3 (d) shows the spectrum and the increase in overlapping area compared to the RGB camera, indicating a stronger ability for identifying different wavelengths. The multispectral camera

can also be used to capture near infrared bands, improving its potential to be used in surgical environments.

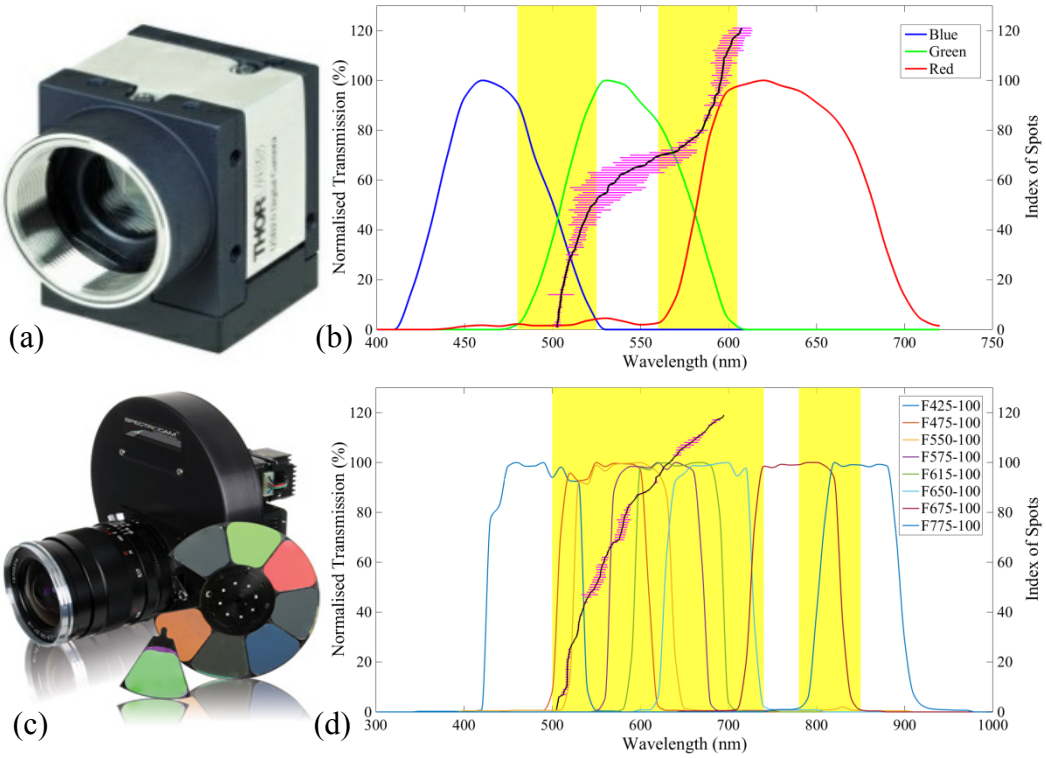

Fig. 3. (a) RGB camera. (b) Normalised filter transmission spectra for the RGB camera and the overlapping area (yellow shadow), together with estimated wavelengths (black) and the corresponding error bar (cyan). (c) Multispectral camera. (d) Filter transmission spectra for the multispectral camera and the overlapping area (yellow shadow), together with estimated wavelengths (black) and the corresponding error bar (cyan).

In order to intuitively demonstrate the superiority of the multispectral camera to the RGB camera in colour discrimination ability, both the cameras were applied to capture SL images on a white plane. The colour vectors were recorded for all the spots, and consequently their corresponding wavelengths were estimated using a lookup table of filter transmission ratios generated from the spectra shown in Fig. 3 (b) and (d). The estimated wavelengths were sorted in ascending order and plotted together with the estimation error and the camera filter transmission curves. The result showcases the difference between two cameras: due to the smaller spectral overlapping area, the colour estimation for the RGB camera image suffers from larger errors, and those colours in the blue end are not estimated correctly since there are rarely responses for the green and red channels in that band. On the contrary, the multispectral camera has a larger overlapping spectral area, leading to a much lower estimation ambiguity, and a much wider effective discriminable band.

2.4 Light pattern decoding

In order to reconstruct the 3D surface of the object, the image coordinates of all the spots should be found. In this work, spot centroid positions are considered as their image coordinates.

Pre-processing of the captured SL images is required due to the strong light-tissue interaction. The specular highlights are removed by taking the following steps in sequence: high intensity area detection to find the highlights; morphological transformation and interpolation to replace the intensities of pixels in the highlighted areas with those in the surrounding areas; Gaussian filtering ($\sigma = 1$, kernel size 7×7) to smooth the images. Finally the colour vectors of all the pixels are calculated using the pre-processed images.

In stereoscopy, feature detection and matching is an essential step [20]. Searching for spot centroids in SL images by segmentation can be seen as feature detection. It can be found from Fig. 4 that: the spots generally have similar sizes; in some cases the spots are closely distributed, overlapping each other; spots with shorter wavelengths are generally darker, and their colour could be "contaminated" by nearby brighter spots due to light diffusion; there are even some "missing" spots due to damaged fibres. For instance, the blank area of the SL image on the tissue in Fig. 4 (a) is caused by either darker blue or "missing" spots. Based on these image conditions, we propose a spot segmentation method based on the "normalized cut" algorithm. This approach, developed by Shi and Malik, treats image segmentation as a graph partitioning problem, by setting a criterion according to inter-group difference and intra-group similarity [16]. They formulated this into a simple spectral clustering problem by using the similarity matrix of a graph and standard linear algebra to cluster data points according to the eigenvectors of matrices, leading to better performance compared to some traditional clustering algorithms like k-means [21]. To deal with the SL images firstly a mask is used to make sure that the normalized cut is only applied in the foreground which contains spots. This mask is generated based on regional maxima detection and a morphological transform in order to cover as many spots (foreground) as possible. Then spectral clustering is applied to the pixels inside this mask to cluster them into different spots. Based on the previous works on spectral clustering [22], the steps are listed as follows:

1. Resize the image using a scaling factor of 0.5 to reduce the pixel number and accelerate the computation.
2. Use all the pixels in the mask to build a weighted graph $G = (V, E)$ by establishing a similarity matrix W. One entry of the matrix $w_{i,j}$ represents the similarity between two pixels i and j, and is defined as:

$$w_{i,j} = e^{\frac{-\theta_{ij}{}^2}{\epsilon_1{}^2}} * \begin{cases} e^{\frac{-\|X_i - X_j\|^2}{\epsilon_2{}^2}} & \text{if } \|X_i - X_j\| < r \\ 0 & \text{otherwise} \end{cases}, \quad (2)$$

where X_i and X_j stand for the image coordinates of the pixels, r is the threshold of the Euclidian distance between two pixels, ϵ_1 and ϵ_2 are used to tune the factor weights of colour difference and spatial distance in computing the similarity $w_{i,j}$. A distance threshold r is set to constrain the calculation of $w_{i,j}$ only take place between pixels close to each other, speeding up the computation. r, ϵ_1 and ϵ_2 are normally set empirically, and in this work the typical values used are 3, 0.2, and 5, respectively.

3. Calculate K eigenvectors corresponding to K largest eigenvalues of:

$$D^{-\frac{1}{2}}(D - W)D^{-\frac{1}{2}}x = \lambda x, \quad (3)$$

where D is a diagonal matrix, whose (i, i) entry is the sum of W's ith row, K is the number of clusters. In experiments K can be set automatically according to the number of detected local regional maxima.

4. Stack the K eigenvectors $v_1, v_2, \ldots, v_K$ in columns to form a matrix A, and normalise it in row direction.
5. Use k-means to cluster the rows in A, so all the rows/pixels are labelled.

In this way, the spots are clustered and segmented in the SL image (Fig. 4 (b)).

Spot identification for this SL system is equivalent to the feature matching procedure. The aim is to find the correspondences between the projector image plane and camera image plane. In this work, a reference image on which all the spots are manually identified beforehand is used. By comparing it to the captured SL image, unique labels should be assigned to individual detected spots. Colour is the main information that can be made use of in order to discriminate different spots. Due to the limitations related to light diffusion and detection of low brightness signals mentioned earlier, identifying those spots only according to colour is highly difficult as they result in uncertainty in the colour vector. Thus, an algorithm based on colour and neighbourhood information has been developed:

1. Find neighbours for all the spots in both the reference and SL images based on a Delaunay triangulation (Fig. 4 (b)).
2. Calculate the average colour vector, and establish a stack of neighbours' colour vectors in a clockwise sequence for every spot.
3. Compare the colour vectors of the spot of interest and its neighbours to determine unique matches between the SL image and the reference image.
4. The spot matching procedure is propagated from the initially identified spots to their neighbours based on to colour information and local rigid registration. (Fig. 4 (c, d)). Thus, the spots are identified and matched to the rays emitted from the probe.
5. Remove incorrect spot-ray correspondences according to the calibration.

Together with the calibration results, the tissue surface can be recovered.

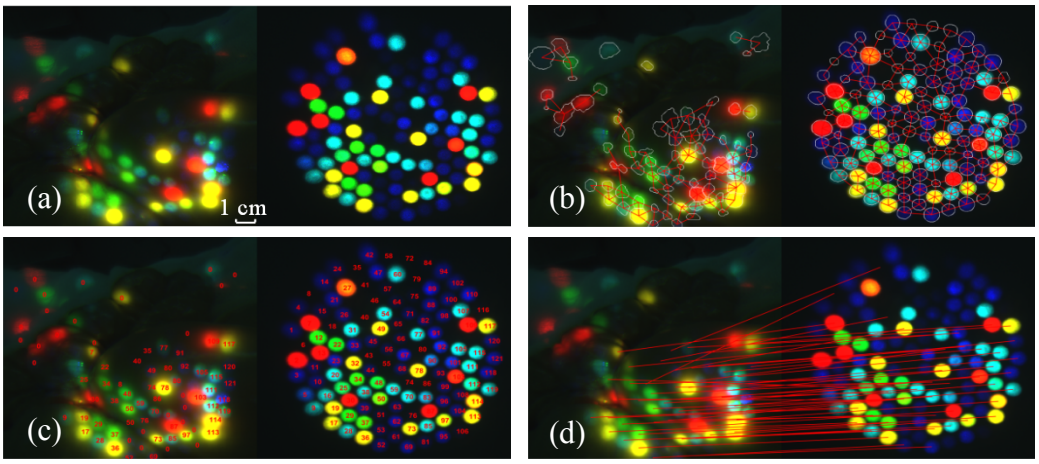

Fig. 4. (a) The SL image (left) and the reference image (right). (b) Neighbour detection for the SL image (left) and reference image (right): segmented spot boundaries (white) and connections between neighbours (red). (c) Labelled SL image (left) according to the labels assigned manually in the reference image (right). (d) Correspondences of spots between the SL image (left) and the reference image (right).

3. Experimental results

In order to evaluate the feasibility of the software platform and its practicality, experiments on different objects have been carried out including a heart phantom and porcine large bowel during an *in vivo* animal trial to test the device in a challenging clinical environment. Rather than inserting the probe through the biopsy channel, the probe was mounted on a rigid support, and the SL images captured by a multispectral and an RGB camera (each coupled to a rigid endoscope). The angle between the probe and each camera was about 10-15°, the

baseline about 5 cm, and the optical axis of both endoscopes roughly perpendicular to the object surface. Images were acquired at 30 FPS, with a maximum 33 ms exposure time per frame. Every consecutive 8 frames from the multispectral camera formed one image stack. Practically this fame rate is high enough to avoid image blurring caused by respiration movements. It takes ~50 s to process a single frame using Matlab (Intel i7-3770, 8 GB RAM). The results are structured into two parts: evaluation of pattern decoding algorithm using multispectral and RGB cameras; effect of pattern decoding on reconstruction accuracy.

3.1 Light pattern decoding using multispectral and RGB cameras

Given an accurate calibration, the light pattern decoding results determine the reconstruction accuracy. Here results using both the cameras are demonstrated. As light pattern decoding is divided into spot detection and identification, images acquired from phantom and *in vivo* experiments are used to evaluate the performance of these two steps. The indicators used include the sensitivities and specificities of detection and identification results. These are calculated by comparison with the ground truth data (manual decoding results). Given the automatically detected number T_{da}, the manually detected number T_{dm}, and the correctly automatically detected number T_{dc}, the sensitivity of spot detection is defined as $Sen_d = \frac{T_{dc}}{T_{dm}}$, and the precision as $Pre_d = \frac{T_{dc}}{T_{da}}$. Given the automatically identified number T_{ia}, the manually identified number T_{im}, and the correctly automatically identified number T_{ic}, the sensitivity of spot identification is defined as $Sen_i = \frac{T_{ic}}{T_{im}}$, and the precision as $Pre_i = \frac{T_{ic}}{T_{ia}}$. The average and standard deviation of these indicators in different experiments are shown in Fig. 5.

The multispectral camera was used to capture eight SL images of a heart phantom and ten SL images of the porcine large bowel, while the RGB camera acquired five for heart phantom and nine for porcine large bowel.

Pattern decoding aims to achieve identification precisions as high as possible while maintaining identification sensitivities. These criteria can guarantee optimum performance for surface reconstruction. Taking all the SL images (Fig. 5) into consideration, our algorithm leads to identification sensitivities higher than 50% and precisions higher than 90% in 28 out of 32 measurements.

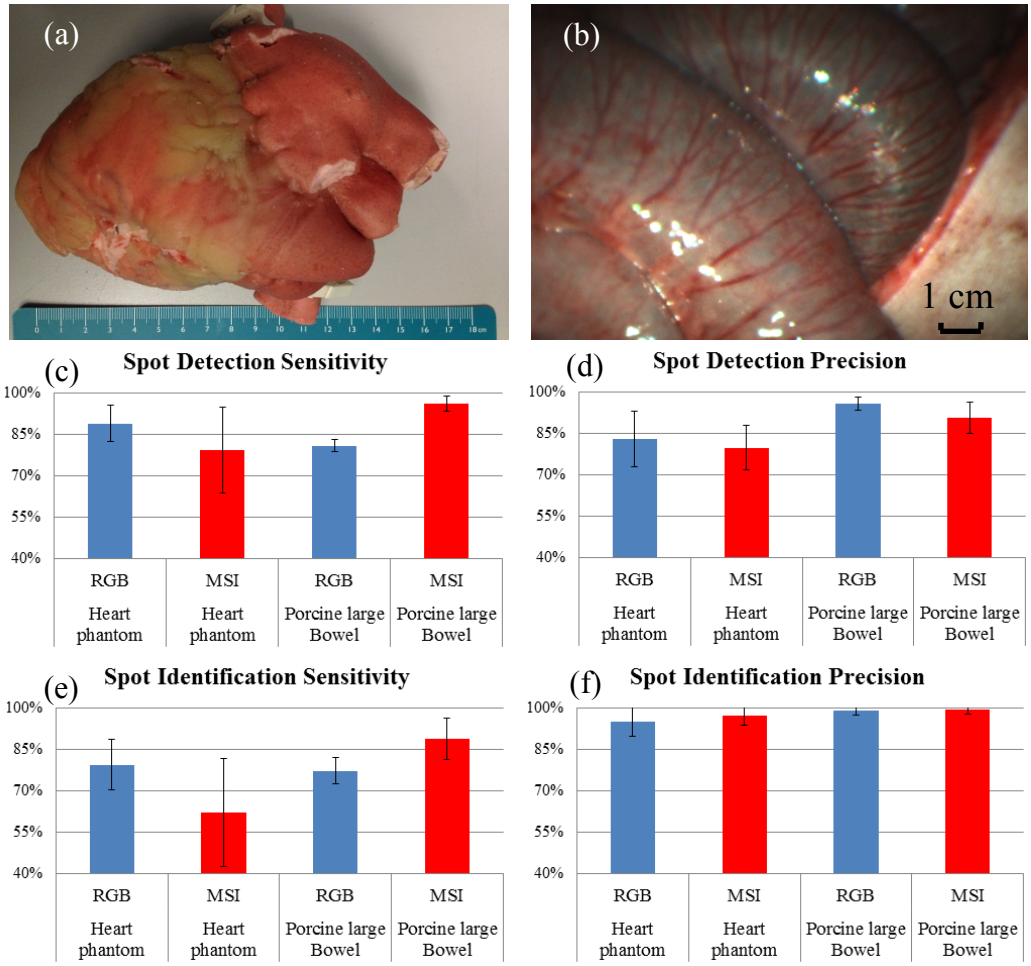

Fig. 5. (a) The heart phantom. (b) The porcine large bowel sample. (c) Spot detection sensitivity. (d) Spot detection precision. (e) Spot identification sensitivity. (f) Spot identification precision.

The results show the robustness of the spot detection algorithm. For all the images, the average sensitivities are always higher than 75% (Fig. 5 (c)), while the average precisions are higher than 80% (Fig. 5 (d)). According to some trials in which parts of spots are manually set to "unidentified", it is found that 50% sensitivity and 70% precision in detection is already enough for the identification step. Therefore, this detection algorithm is reliable in practice. Inevitably, the identification sensitivities are slightly lower than the detection results, but the identification precisions are higher for all cases. The average identification precisions for all the SL images are higher than 95% for both cameras. In practice those SL image with low identification precision can be detected and abandoned, so very little error will be introduced even if the identification fails occasionally.

The light pattern decoding results of the two cameras on the heart phantom and the porcine large bowel in the *in vivo* experiment are shown in Fig. 5. In the phantom experiment, both of the cameras performed well. The RGB camera led to

higher identification sensitivity, while the multispectral camera outperforms in identification precision. Although both of them work well in the *in vivo* experiment, the multispectral camera outperforms the RGB camera in both identification indicators, especially precision. This is due to the high importance of colour information in the spot identification step. As the multispectral camera has undoubtedly much higher colour discrimination ability, it leads to better identification results. The experimental results also indicate that our algorithm can be affected by many factors such the surface texture, topology and background illumination. More experiments are in progress to investigate whether the multispectral camera is superior in practice.

3.2 Surface reconstruction accuracy

The heart phantom has been used to measure the reconstruction accuracy. The surface mesh measured by an MCAx25+ handheld laser scanner is used as the ground truth. Eight SL images of the heart phantom from different angles are captured, so eight reconstructed surfaces can be acquired separately using manual and automatic pattern decoding methods. By registering the ground truth mesh and the reconstructed surface using the rigid iterative closest point (ICP) method [23] the reconstruction error can be calculated as the distance between these two registered surfaces (Fig. 6). The average and the maximum distance are used as the indicators. The result of using the automatic decoding is compared to that of manual pattern decoding to test the influence of the pattern decoding algorithm.

Table 1 showcases the reconstruction result using manual light pattern decoding. The statistics demonstrate that the accuracy of surface reconstruction using the SL system under strict calibration and perfect pattern decoding is very high, with average error smaller than 0.7 mm and maximum errors under 3 mm from seven out of eight SL images. It also shows that the reconstruction accuracy drops if the automatic pattern decoding algorithm is adopted. However, if the case where identification precision was lower than 90% is excluded, the mean values of the average distance and maximum distance reach 0.7 mm and 2.98 mm, respectively, making a very small difference from the results using manual pattern decoding. Given that satisfactory identification results (sensitivity > 50% and precision > 90%) can be achieved in 87% of SL images the robustness and accuracy of surface reconstruction using the proposed algorithm is demonstrated.

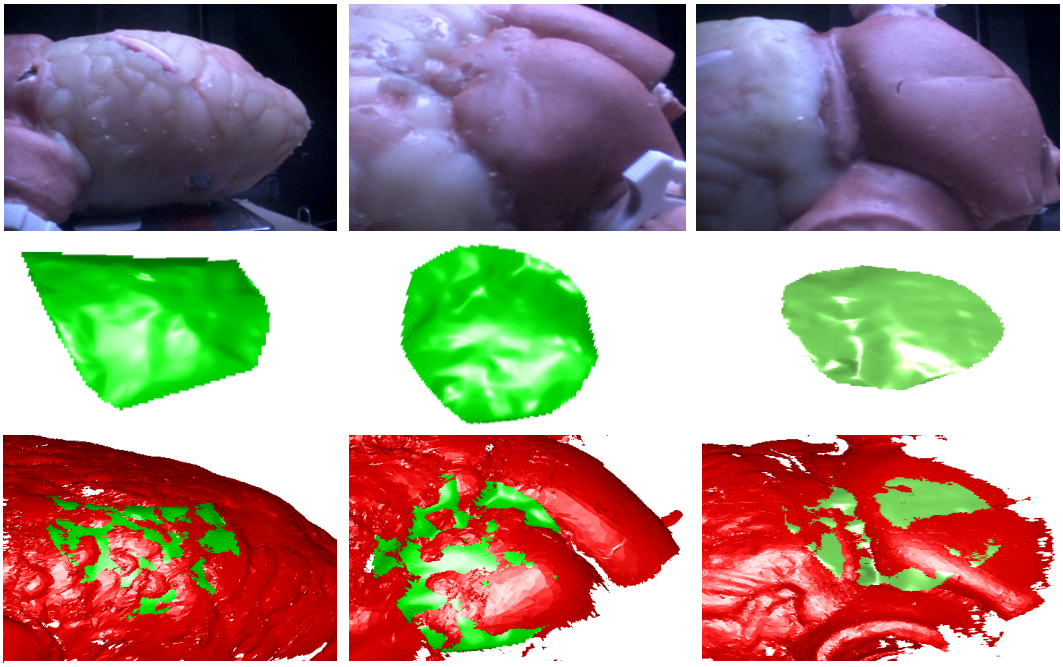

Fig. 6. ICP-based rigid registration to evaluate the reconstruction error. First row: silicone heart phantom under white light; second row: the reconstructed surface; third row: registration of the reconstructed surface (green) with the ground truth mesh (red).

Table 1. Heart phantom surface reconstruction accuracy using manual and automatic pattern decoding. The overall median, average, and maximum value (column header) of the average, standard deviation, and maximum errors for all the reconstructed surfaces (row header) are listed.

	Identification sensitivity	Identification precision	Mean error (mm)	Std error (mm)	Max error (mm)
(Manual) Median	100.00%	100.00%	0.65	0.32	2.52
(Manual) Mean	100.00%	100.00%	0.64	0.35	2.78
(Manual) Max	100.00%	100.00%	0.72	0.44	5.04
(Automatic) Median	70.51%	98.33%	0.71	0.40	3.08
(Automatic) Mean	68.74%	96.70%	0.88	0.67	5.58
(Automatic) Max	90.76%	100.00%	2.17	2.65	23.76

4 Conclusions and future work

This work aimed to improve the practicality of the ICL SL system and demonstrate its potential in MIS environments. In order to enhance light pattern decoding a multispectral camera was proposed. The *in vivo* experiment demonstrated its superiority over the RGB camera in spot identification. The proposed pattern decoding algorithm underwent evaluations using different experiments, showing promising reconstruction results. Since the current light pattern is sparse and the decoding relies on neighbourhood information, the high curvature may lead to decoding failure in some areas. But there are still valid

clinical examples of applications for this SL system, including detection of flat polyps and surgical planning or guidance for organs such as liver or kidney.

Future work will focus on hardware improvements in order to adapt the SL system to MIS environments, such as enhancing the light pattern design and increasing the portability of the system. For instance, the probe and camera could be integrated into the shaft of a laparoscope to improve the portability and simplify the calibration procedure. Furthermore, a real-time medical application is targeted for development, to facilitate augmented reality together with pre-operative data from other imaging modalities like MRI or CT.

Acknowledgements. This project is funded by ERC grant 242991, and the NIHR Imperial Biomedical Research Centre (BRC)/Imperial Innovations Therapeutic Primer Fund (Imperial Confidence in Concept). The authors thank Northwick Park Institute for Medical Research (NPIMR) and German Cancer Research Center (DKFZ) for collaboration in experimental data acquisition. Neil Clancy is supported by an Imperial College Junior Research Fellowship.

Conflict of interest. None of the authors has a conflict of interest.

References

1. Clancy NT, Stoyanov D, Maier-Hein L, Groch A, Yang G-Z, Elson DS (2011) Spectrally encoded fiber-based structured lighting probe for intraoperative 3D imaging. Biomedical Optics Express 2 (11):3119-3128. doi:10.1364/BOE.2.003119

2. Schwartz JJ, Lichtenstein GR (2004) Magnification endoscopy, chromoendoscopy and other novel techniques in evaluation of patients with IBD. Techniques in Gastrointestinal Endoscopy 6 (4):182-188. doi:http://dx.doi.org/10.1016/j.tgie.2004.09.006

3. Maier-Hein L, Mountney P, Bartoli A, Elhawary H, Elson D, Groch A, Kolb A, Rodrigues M, Sorger J, Speidel S, Stoyanov D (2013) Optical techniques for 3D surface reconstruction in computer-assisted laparoscopic surgery. Medical Image Analysis 17 (8):974-996. doi:http://dx.doi.org /10.1016/j.media.2013.04.003

4. King AP, Edwards PJ, Maurer CR, Cunha DAd, Gaston RP, Clarkson M, Hill DLG, Hawkes DJ, Fenlon MR, Strong AJ, Cox TCS, Gleeson MJ (2000) Stereo Augmented Reality in the Surgical Microscope. Presence: Teleoper Virtual Environ 9 (4):360-368. doi:10.1162/105474600566862

5. Geng J (2011) Structured-light 3D surface imaging: a tutorial. Adv Opt Photon 3 (2):128-160. doi:10.1364/AOP.3.000128

6. Ackerman JD, Keller K, Fuchs H (2002) Surface reconstruction of abdominal organs using laparoscopic structured light for augmented reality, vol 4661. Society of Photo-Optical Instrumentation Engineers, Bellingham, WA, INTERNATIONAL

7. Chan M, Lin W, Zhou C, Qu JY (2003) Miniaturized three-dimensional endoscopic imaging system based on active stereovision. Appl Opt 42 (10):1888-1898. doi:10.1364/AO.42.001888

8. Wu TT, Qu JY (2007) Optical imaging for medical diagnosis based on active stereo vision and motion tracking. Opt Express 15 (16):10421-10426. doi:10.1364/OE.15.010421
9. Maurice X, Albitar C, Doignon C, de Mathelin M A structured light-based laparoscope with real-time organs' surface reconstruction for minimally invasive surgery. In: Engineering in Medicine and Biology Society (EMBC), 2012 Annual International Conference of the IEEE, Aug. 28 2012-Sept. 1 2012 2012. pp 5769-5772. doi:10.1109/EMBC.2012.6347305
10. Schmalz C, Forster F, Schick A, Angelopoulou E (2012) An endoscopic 3D scanner based on structured light. Medical Image Analysis 16 (5):1063-1072. doi:http://dx.doi.org/10.1016/j.media.2012.04.001
11. Sorg BS, Moeller BJ, Donovan O, Cao Y, Dewhirst MW (2005) Hyperspectral imaging of hemoglobin saturation in tumor microvasculature and tumor hypoxia development. BIOMEDO 10 (4):044004-044004-044011. doi:10.1117/1.2003369
12. Tracy CR, Terrell JD, Francis RP, Wehner EF, Smith J, Litorja M, Hawkins DL, Pearle MS, Cadeddu JA, Zuzak KJ (2010) Characterization of renal ischemia using DLP hyperspectral imaging: a pilot study comparing artery-only occlusion versus artery and vein occlusion. J Endourol 24 (3):321-325. doi:10.1089/end.2009.0184
13. Yang VXD, Muller PJ, Herman P, Wilson BC (2003) A multispectral fluorescence imaging system: Design and initial clinical tests in intra-operative Photofrin-photodynamic therapy of brain tumors. Lasers in Surgery and Medicine 32 (3):224-232. doi:10.1002/lsm.10131
14. Xu H, Rice BW (2009) In-vivo fluorescence imaging with a multivariate curve resolution spectral unmixing technique. BIOMEDO 14 (6):064011-064011-064019. doi:10.1117/1.3258838
15. Soille P (2003) Morphological Image Analysis: Principles and Applications. Springer-Verlag New York, Inc.,
16. Shi J, Malik J (2000) Normalized cuts and image segmentation. Pattern Analysis and Machine Intelligence, IEEE Transactions on 22 (8):888-905. doi:10.1109/34.868688
17. Heikkila J, Silven O A four-step camera calibration procedure with implicit image correction. In: Computer Vision and Pattern Recognition, 1997. Proceedings., 1997 IEEE Computer Society Conference on, 17-19 Jun 1997 1997. pp 1106-1112. doi:10.1109/CVPR.1997.609468
18. Zhang Z (2000) A flexible new technique for camera calibration. Pattern Analysis and Machine Intelligence, IEEE Transactions on 22 (11):1330-1334. doi:10.1109/34.888718
19. Li Q, Dai C, Liu H, Liu J Leukemic cells segmentation algorithm based on molecular spectral imaging technology. In, 2009. pp 73830V-73830V-73837
20. Szeliski R (2010) Computer Vision: Algorithms and Applications. Springer-Verlag New York, Inc.,
21. Ng A, Jordan M, Weiss Y (2001) On spectral clustering: Analysis and an algorithm. doi: citeulike-article-id:1158897
22. Von Luxburg U (2007) A tutorial on spectral clustering. Stat Comput 17 (4):395-416. doi:10.1007/s11222-007-9033-z
23. Zhang Z (1994) Iterative point matching for registration of free-form curves and surfaces. Int J Comput Vision 13 (2):119-152. doi:10.1007/BF01427149